TITLE:

Diagnostics of Shock Tube Flows by Laser Interferometry

AUTHOR(S):

TOYOTA, Tetsurou; NISHIDA, Michio

CITATION:

TOYOTA, Tetsurou ...[et al]. Diagnostics of Shock Tube Flows by Laser Interferometry. Memoirs of the Faculty of Engineering, Kyoto University 1982, 44(3): 410-429

ISSUE DATE:

1982-10-30

URL:

http://hdl.handle.net/2433/281221

RIGHT:

京都大学学術情報リポジトリ
KURENAI 紅
Kyoto University Research Information Repository

Diagnostics of Shock Tube Flows by Laser Interferometry

By

Tetsurou TOYOTA and Michio NISHIDA

(Received March 27, 1982)

Abstract

In this paper, the diagnostics of shock tube flows by a laser differential interferometer using Wollaston prisms is described. This method has some advantages. It can apply to a case in which the optical path change is only a small fraction of the wave length, and the influence of vibration and laser ripple can be suppressed whereby excellent resolutions in space and time are obtained. In the present work, this method was applied to the measurements of the density change across a shock generated in a shock tube and a shock Mach number. From the investigations of the incident shock, reflected shock and contact surface, it was concluded that the influence of the boundary layer on the side and end wall becomes large when the initial pressure in the test chamber is less than 1.0 kPa. It was also concluded that a strong interaction of the reflected shock with the side-wall boundary layer is caused for air. Through these experiments, a technique of the density measurement by means of this interferometer has been established. It was confirmed that this method is an excellent way for density measurements in a case where the density change is very small.

1. Introduction

Interferometry has been often used as being most appropriate for density measurements. Most conventional ways are such that the optical path change between a test beam and a reference beam caused by a density perturbation in the flow is observed as a perturbation of the fringe pattern on an interferogram. Therefore, a quantitative measurement is difficult when the density perturbation becomes so small that the optical path change is less than the order of the light wave length.

The laser differential interferometer using Wollaston prisms, developed by Smeets,[1,2] has many advantages. For example, the influence of vibration can be reduced, which is one of the most significant features of interferometry, the time resolution is superior because the interference signals are detected by PIN-photodiodes, and the weak phase objects can be examined because the optical

Department of Aeronautical Engineering.

path change can be resolved to about 0.2 per cent of the wave length.

This laser interferometer is widely applicable to flow diagnostics. Smeets[3] measured the density distribution in the boundary layer behind the shock, using a multi-beam interferometer technique. Lensch[4,5] applied the laser interferometer to the determination of the rotational relaxation time of D_2, using a cryogenic shock tube. This technique was also employed for the diagnostics of reflected shock waves.[6] It is possible to measure the local density gradients by making the distance between the reference and test beams small. By traversing the laser beams across an axisymmetric flow and by using an Abel inversion, the local density at any position of the axisymmetric flow can be evaluated.

In this work, as the first stage, the laser differential interferometer has been applied to the measurements of the density changes across the incident and reflected shocks, and the shock Mach numbers of both shocks. The speed of the contact surface has also been investigated by this technique.

2. Principle of Laser Differential Interferometry

A schematic diagram of an optical system is shown in Fig. 1. The system is based on the same type of differential interferometer, using Wollaston prisms as a

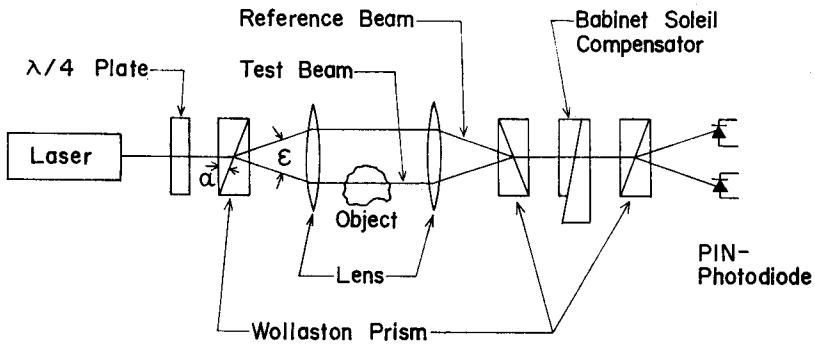

Fig. 1. Optical System.

beam splitter, as developed by Smeets.[1] The linear polarization of the original laser beam is transformed into a circular polarization by means of a $\lambda/4$ plate in order to be free from any orientation of the following Wollaston prism. (Appendix A) The laser beam travels through the first Wollaston prism which is made of uniaxial birefringent crystal, and is split into two beams having a perpendicular polarization. The split angle ε ($\ll 1$) is given by

$$\varepsilon = 2|n_{ex} - n_0| \tan \alpha$$

where α is the prism angle, and n_0 and n_{ex} are the ordinary and extraordinary

refractive indices of the material of the prism, respectively. The refractive indices of typical uniaxial birefringent crystals are shown in Table 1. A lens is placed at the distance of its focal length from the Wollaston prism, whereby the two beams

Table 1. Refractive Indices of Uniaxial Birefringent Crystal

	n_0	n_{ex}
Calcite	1.655	1.485
Quartz	1.544	1.555

become parallel with each other in the test section. One of these beams works as a test beam, and the other is used as a reference beam. The distance between the two beams can be set up arbitrarily by changing the focal length of the lens. The two partial beams pass through the test object, and an optical path change is caused between the two beams by perturbation in the density. Then, the beams are recombined by means of a lens having the same focal length as the first lens, and the same Wollaston prism as the first prism. The orientation of the axes of the first and second prisms is the same. After passing through the second Wollaston prism, the partial beams are recombined and have a common path, but they are still polarized perpendicularly so that they cannot yet interfere. By means of a Babinet-Soleil compensator whose axes are aligned with the polarization directions, the relative phase difference between the beams which are polarized perpendicular to each other, can be controlled. Finally, the partial beams are mixed by a third Wollaston prism whose axes are arranged θ with respect to the polarization of the beams, and are split into two interfering pairs of beams. These two beams are received by two separate photodiodes. When the polarization directions of the two partial beams are in the directions of the y- and z-axes (Fig. 2)

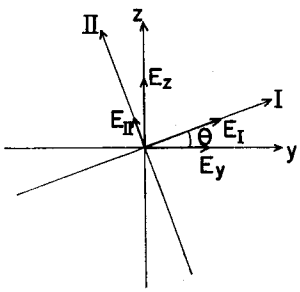

Fig. 2. Axes of Prism.

until the last Wollaston prism is reached, their optical disturbances are represented in the form

$$E_y = P_y \cos\left(\frac{2\pi}{\lambda}x\right), \quad E_z = P_z \cos\left[\frac{2\pi}{\lambda}(x+\Delta\Phi)\right],$$

where x has been taken in the direction of the beam propagation, and y and z have been taken perpendicular to x, and $\Delta\Phi$ is the relative optical path difference between the beams, λ the wave length, P_y and P_z the amplitude of the beams. By means of the last Wollaston prism, the partial beams are mixed and are transformed into two interfering pairs of beams. If their polarization directions are in the I- and II-directions, the beams E_{I} and E_{II} are given by the I-component of E_y and E_z, and the II-component of E_y and E_z, respectively:

$$\begin{aligned} E_{\mathrm{I}} &= E_y \cos\theta + E_z \sin\theta \\ &= (A^2+B^2)^{1/2} \cos\left(\frac{2\pi}{\lambda}x - \tan^{-1}\frac{B}{A}\right), \end{aligned} \tag{1}$$

$$\begin{aligned} E_{\mathrm{II}} &= -E_y \sin\theta + E_z \cos\theta \\ &= (C^2+D^2)^{1/2} \cos\left(\frac{2\pi}{\lambda}x - \tan^{-1}\frac{D}{C}\right), \end{aligned} \tag{2}$$

where A, B, C, D are given as follows, respectively:

$$A = P_y \cos\theta + P_z \sin\theta \cos\left(\frac{2\pi}{\lambda}\Delta\Phi\right),$$

$$B = -P_z \sin\theta \sin\left(\frac{2\pi}{\lambda}\Delta\Phi\right),$$

$$C = -P_y \sin\theta + P_z \cos\theta \cos\left(\frac{2\pi}{\lambda}\Delta\Phi\right),$$

$$D = -P_z \cos\theta \sin\left(\frac{2\pi}{\lambda}\Delta\Phi\right).$$

The beam intensity is in proportion to a square of the amplitude of the beam. The intensities of E_{I} and E_{II}, I_{I} and I_{II}, respectively, are then

$$\begin{aligned} I_{\mathrm{I}} &= A^2+B^2 \\ &= 2P_yP_z \sin\theta\cos\theta\cos\left(\frac{2\pi}{\lambda}\Delta\Phi\right) + P_y^2\cos^2\theta + P_z^2\sin^2\theta, \end{aligned}$$

$$\begin{aligned} I_{\mathrm{II}} &= C^2+D^2 \\ &= -2P_yP_z \sin\theta\cos\theta\cos\left(\frac{2\pi}{\lambda}\Delta\Phi\right) + P_y^2\sin^2\theta + P_z^2\cos^2\theta, \end{aligned}$$

Thus the intensities vary as a function of the optical path difference. The difference between I_{I} and I_{II} is given by

$$I_{\mathrm{I}}-I_{\mathrm{II}} = 4P_yP_z \sin 2\theta \cos^2\left(\frac{\pi}{\lambda}\Delta\Phi\right) + (P_y^2-P_z^2)\cos 2\theta - 2P_yP_z \sin 2\theta \,. \tag{3}$$

The quantity $I_{\mathrm{I}}-I_{\mathrm{II}}$ is detected by PIN-photodiodes, which respond linearly over a wide range of the beam intensity. The voltage U generated by the detector is, therefore, given by

$$U = U_0 \cos^2\left(\frac{\pi}{\lambda}\Delta\Phi\right) + U_1 \,, \tag{4}$$

where U_0 and U_1 are the constants dependent on the laser power, the angle θ, and the properties of the photodiodes. Consequently, the change of the optical path difference is observed by a change of voltage.

The variation of density can be obtained from a variation of output voltage. Let L be the width of the test section, n be the refractive index and let the subscripts 1 and 2 represent the values on the reference and test beams, respectively. Then, the optical path difference of the beams in the test section is given by

$$\Delta\Phi/\lambda = (L_2n_2-L_1n_1)/\lambda = L(n_2-n_1)/\lambda \,. \tag{5}$$

Since the Gladstone-Dale formula is expressed as

$$n-1 = K\rho/\rho_0 \,,$$

the relation between the density difference and the optical path difference is obtained as follows:

$$\frac{\Delta\Phi}{\lambda} = \frac{KL}{\lambda}\frac{\rho_2-\rho_1}{\rho_0} \,, \tag{6}$$

where ρ_0 is the density at the standard state (273 K, 1 atm), and K is the non-dimensional Gladstone-Dale constant for the standard state. The values of the Gladstone-Dale constants for the gases used in this experiment are shown in Table. 2.

Table 2. Gladstone-Dale Constant

Gas	K ($\times 10^{-4}$)
Ar	2.81
Air	2.92

The relation between the output voltage U and the density difference $\Delta\rho$ ($=\rho_2-\rho_1$) is obtained from Eqs. (4) and (6):

$$U = U_0 \cos^2\left(\frac{\pi KL}{\lambda}\frac{\Delta\rho}{\rho_0}\right) + U_1 . \qquad (7)$$

In order to obtain $\Delta\rho$ from the experimental values of U by using Eq. (7), the values of K, L, λ, ρ_0 and U_0 must be known. These values, except U_0, can be easily estimated. U_0 can be determined from the interference curve shown in Fig. 3, which has been obtained by using the Babinet-Soleil compensator. The initial optical path difference is also set up by means of this compensator.

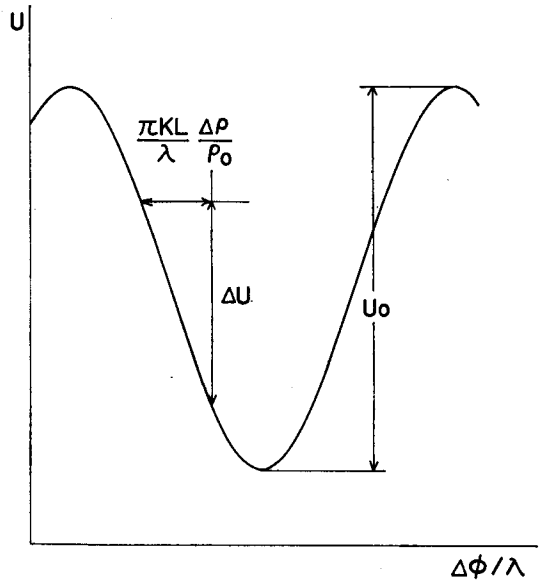

Fig. 3. Interference Curve.

3. Experimental Apparatus and Conditions

The laser differential interferometry has been applied to the diagnostics of shock tube flows. The experimental apparatus and the optical system are shown schematically in Fig. 4. The shock tube is set up vertically, and consists of a 300 mm long high-pressure section and a low-pressure section whose length is variable between 906 mm and 1196 mm. Both sections are made of stainless steel tubes with an inner diameter of 38 mm. The windows are 20 mm in diameter and can be placed at distances of 15, 25, 35, 55 or 305 mm from the end wall. Poly (ethylene terephthalate) films are used as diaphragms. To exchange the diaphragm is possible in a short time by means of the rolling-up apparatus as shown in the figure.

The optical system is the same as shown in Fig. 1. A linear polarized He-Ne

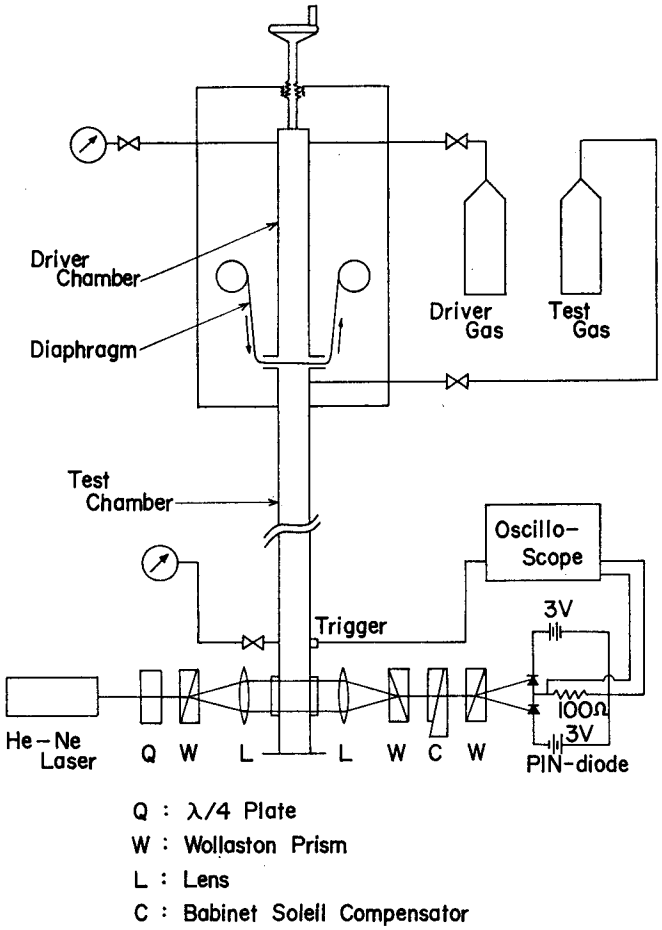

Fig. 4. Experimental Apparatus.

laser (NEC GLG5700, 25 mW, λ=6328 Å) was used as a light source. The beam splitting angle ε of the Wollaston prism (Calcite) was 3.9°, and the distance between the partial beams in the test section was 13.6 mm. The beams were adjusted perpendicular to the axis of the shock tube, and polarized vertically and horizontally. The optical axes of the third Wollaston prism were arranged at 45° with respect to the polarization of the beams. It is obvious from Eqs. (3) and (4) that the output of the voltage U_0 is maximum in this condition.

PIN silicon photodiodes (Hamamatsu TV S-1190-01) were used as the detector. They respond linearly over a wide range of the intensity of the beam, and the rise time is of the order of 1 ns. The outputs of U were observed on an oscilloscope (TEKTRONIX 7623A), which was triggered by a piezo pressure gauge (Kistler 601A).

The relation between U and $\Delta\Phi/\lambda$ was examined prior to the experiments, by means of a Babinet-Soleil compensator, and the result is shown in Fig. 5.

Driver gas/test gas was Ar/Ar or N_2/Air. The experiments were carried out in the range of the initial pressure p_1 from 0.1 to 2.1 kPa (0.78 to 15.6 torr). The shock Mach number was varied by using diaphragms of various thickness.

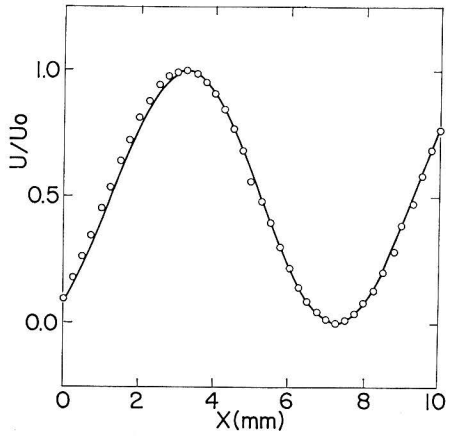

Fig. 5. Measured Values of U.

4. Results and Discussion

4.1. Incident Shock

4.1.1. Density Signal by Incident Shock

The density signals caused by the incident shock are shown in Figs. 6 and 7. When the shock arrives at the first beam (test beam), the voltage U varies. That is, the optical path difference between the two beams is changed because the

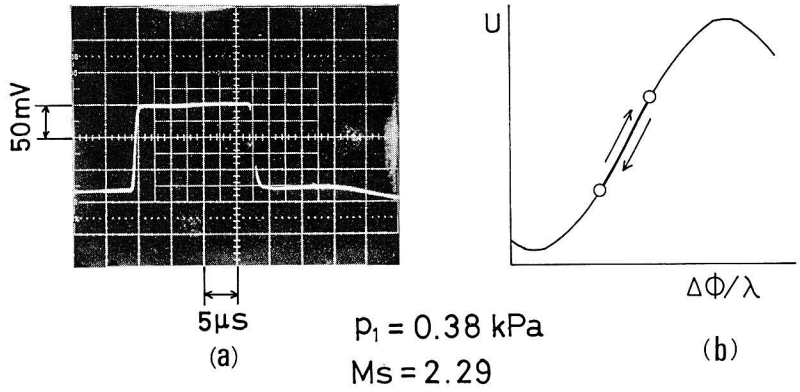

Fig. 6. Output Signal.

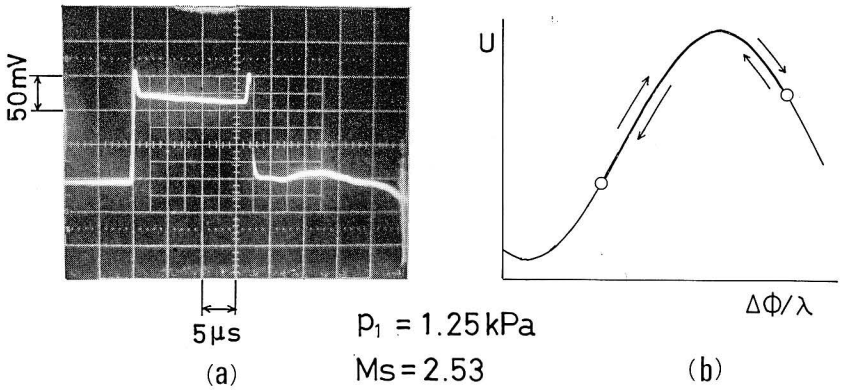

Fig. 7. Output Signal.

test beam traverses in the flow region behind the shock, and the reference beam travels in the region ahead of the shock. This state continues until the reference beam is reached by the shock. After the shock passes across the second beam, both beams are in the region behind the shock, so that the density difference disappears and the voltage signal returns to the initial value. Therefore, the density difference can be calculated from the voltage variation. From the duration time of the signal, the velocity of the shock can be also calculated.

The condition of Fig. 6 is such that the initial pressure $p_1=0.38$ kPa, the shock Mach number $M_s=2.29$ and the test gas is air. The path of the voltage variation caused by the optical path change is shown in Fig. 6(b). This result gives the density ratio $\rho_{21}=3.07$, and the deviation from the ideal value given by the Rankine-Hugoniot relation is 0.75 %. In this case, the optical path change is equivalent to 12.9 % of the wave length of the laser beam. In the case of Fig. 7, the test gas is air, and $p_1=1.25$ kPa, $M_s=2.53$. The change in the optical path is larger than that in the case of Fig. 6, so that the signal becomes complicated. The density ratio is calculated to be $\rho_{21}=3.55$ and the deviation is 5.4 %. The change in the optical path difference is equivalent to 53.6 % of the wave length of the laser beam.

4.1.2. Rise Time of Output

In the case of Ar, the observed average rise times are 0.9, 0.85 and 0.8 μs corresponding to the initial pressure of 0.1, 0.31 and 0.52 kPa, respectively. When the initial pressure is 1.0 kPa or more, the time is in the range from 0.75 to 1.0 μs. To explain these phenomena, the thickness and curvature of the shock, and hence the spatial resolution should be taken into account. We consider this for the case of Ar.

The shock thickness can be estimated in relation to the mean free path ahead

of the shock and the shock Mach number.[7] The mean free path is given in the form

$$l = 16\mu/5n(2\pi mkT_1)^{1/2},$$

where μ is the viscosity, n the number density, m the mass of the molecule and k the Boltzmann constant. Under the conditions of the present experiments, the shock has a maximum thickness at $p_1=0.1$ kPa. Under this condition, the thickness becomes about four times as large as the mean free path. The estimated rise time of the output voltage is about 0.26 μs at $M_s=3.2$, meaning that it is smaller than the observed times. Hence, the effect of the shock thickness is not significant.

Next, we consider the curvature of the shock.[8] This can be estimated in relation to the Reynolds number $Re=a_1R/\eta_1$, where a_1 is the velocity of sound, η_1 is the kinetic viscosity in the undisturbed region ahead of the shock and R is the radius of the shock tube. At Reynolds numbers up to 1000, the shock wave is nearly symmetrical, and the curvature decreases with the Reynolds number. Under the conditions of the present experiments, the shock has a maximum curvature at $p_1=0.10$ kPa. If the Mach number is 3.2, the rise time of the output will be 0.86 μs. When the Reynolds number is more than 1000, the shape of the shock front becomes complex and there exist local portions of the shock with a considerable curvature and an inclination of the shock front with respect to the tube axis. For $p_1=1.0$ kPa, the Reynolds number is 4900, and in this case the shock front has a width about 1 mm according to the work done by Liepmann and Bowman.[8] This gives the rise time of 1.3 μs for $M_s=2.6$. Therefore, this suggests that the shock shape has some influence on the rise time.

Over the test length L, a laser beam diameter (based on $1/e^2$ intensity) can be realized that is approximately given by

$$d_0 = \left(\frac{\pi}{2}\lambda L\right)^{1/2}. \tag{8}$$

Under the present conditions, the diameter can be kept approximately at 0.2 mm, but the actual beam diameter can be estimated to be about 0.5 mm. The time required for a discontinued surface in the range of the Mach number 2.0 to 3.2 to cross the beam of 0.5 mm diameter is 0.5 to 0.8 μs.

From the consideration mentioned above, it may be mentioned that the curvature of the shock front and the diameter of the beam have influence on the rise tiem.

4.1.3 Density Ratio ρ_{21}

The measured density ratio ρ_{21} for the incident shock in argon and air are shown in Fig. 8. The solid lines represent theoretical values from the Rankine-Hugoniot relation. According to the oscillograms, the density behind the shock is not uniform and increases gradually. This increase in the density $\Delta\rho$ is $\Delta\rho/\rho_2=0.05$ at $p_1=0.1$ kPa. This is caused by the deceleration of the incident shock, as mentioned later. The measured values shown in Fig. 8 are those taken immediately behind the shock. The difference between the experimental and the theoretical values are within 7 % for argon and 5 % for air, which are independent of a Mach number. The behavior of the incident shock for each test gas is almost the same.

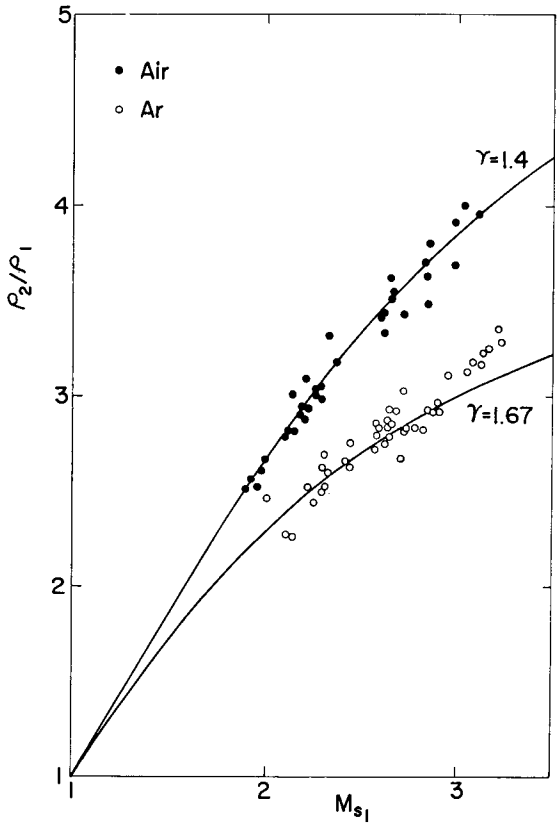

Fig. 8. Incident Shock Density Ratio ρ_{21}.

4.2 Reflected Shock

4.2.1. Density Signal by Reflected Shock

The oscillograms of the reflected shock in argon and in air are shown in Fig. 9.

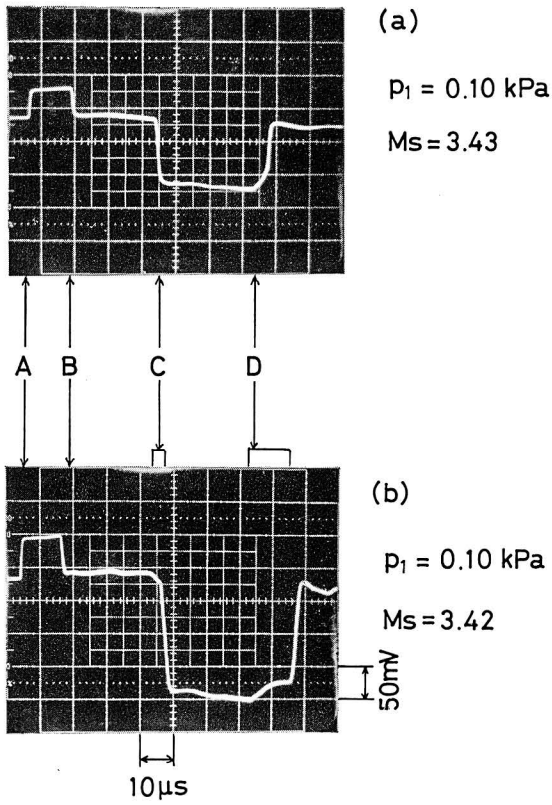

Fig. 9. Output Signal.

At point A, the incident shock arrives at the first beam and a density difference occures, which leads to a change in the optical path difference between the two beams. This continues until the shock reaches the second beam at point B. Thereafter, both of the beams are behind the shock so that the density difference vanishes, and the output signal returns to the initial value. At point C, the reflected shock arrives at the second beam, and then at point D, the shock crosses the first beam. In Fig. 9, the positions of the first and second beams have been taken to be 22 and 8 mm from the end wall, respectively.

4.2.2. Reflected Shock-Boundary Layer Interaction

According to the oscillogram in Fig. 9, the behaviour of the reflected shock in air is different from that in argon. At point C, the density signal changes sharply in argon, while in air such a change is not sharp. At point D, the signal in argon is somewhat rounded, while the behaviour of the signal for air is like a corner-cut. This is because the interaction of the reflected shock with the side-wall boundary layer is more significant in air than in argon. In the boundary

layer, the flow velocity vanishes on the wall, and the reflected shock runs faster in the region close to the wall. When the interaction is small, the shock front has only a curvature near the wall. However, when the interaction is strong, then it is predicted that an oblique shock will appear, and that bifurcation and a boundary layer separation will occur.[9]

The magnitude of such an interaction depends on the relation between the stagnation pressure $p_{bl\cdot stag}$ of the boundary layer (in the reflected shock coordinate) and the free stream pressure p_5 behind the reflected shock. If $p_{bl\cdot stag} > p_5$, the boundary layer passes through the shock and enters smoothly into the region behind the reflected shock, so that the interaction is small. When $p_{bl\cdot stag} < p_5$, however, the stagnant boundary layer fluid separates, and is collected in a bubble that subsequently gets dragged along with reflected shock. The criterion for the production of bifurcation can be calculated as a function of the incident shock Mach number with respect to the ratio of the specific heats γ of the gas. (Appendix B) The relations between $p_{bl\cdot stag}$ and p_5 of argon and air are shown in Fig. 10. Although the present conditions for Ar give $p_{bl\cdot stag} < p_5$ in the range of a

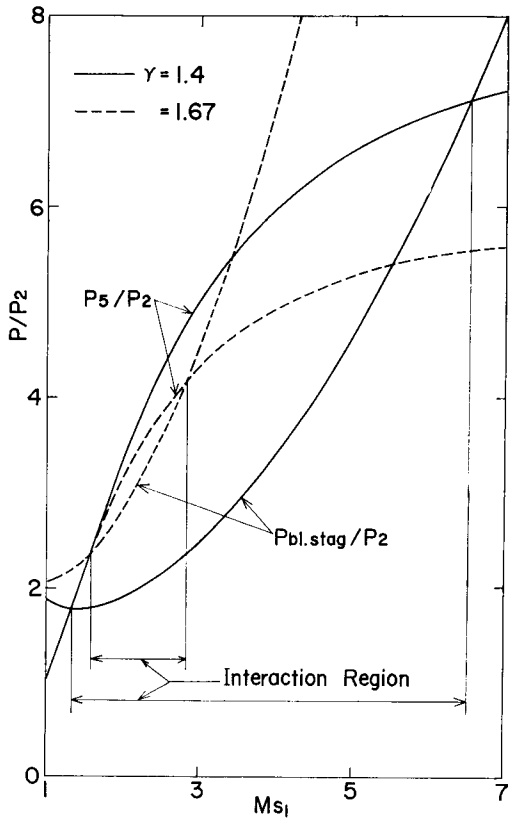

Fig. 10. Relation between $p_{bl\cdot stag}$ and p_5.

Mach number between 1.5 and 2.8, the observed interaction is weak because the difference between $p_{bl\cdot stag}$ and p_5 is relatively small. On the other hand, in air, $p_{bl\cdot stag}<p_5$ over the whole range of our experimental conditions means that the difference between $p_{bl\cdot stag}$ and p_5, is large. Consequently, a strong interaction is observed. The signal change, like the corner-cut shown in Fig. 9(b), is presumably due to the bifurcation of the shock. As the initial pressure increases, the curvature of the shock front in argon becomes small, since the influence of the boundary layer becomes weak.

4.2.3. Reflected Shock Velocity

The results of the reflected shock Mach number are shown in Figs. 11 and 12. The reflected shock Mach number is based on the sound velocity in the

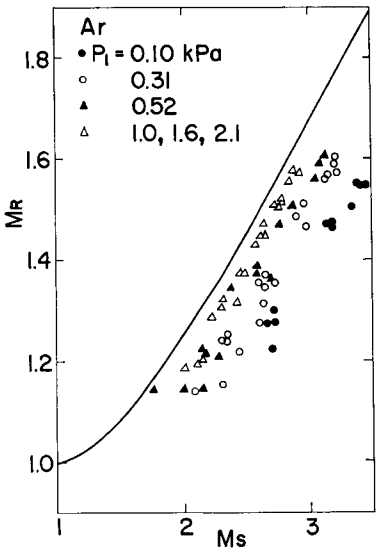

Fig. 11. Measured Reflected Shock Mach Number in Ar.

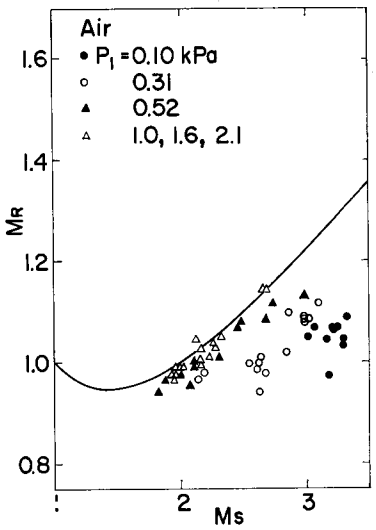

Fig. 12. Measured Reflected Shock Mach Number in Air.

initial temperature. The solid line represents a theoretical curve. The experimental results lie below the theoretical curve and they decrease with the initial pressure. The deviations are approximately 17 % at $p_1=0.1$ kPa, 10 % at $p_1=0.31$ kPa, 7 % at $p_1=0.52$ kPa, and 3 % for $p_1>1.0$ kPa. In air, the measured values are widely scattered compared with those in argon. This is because reading errors occur, since the signals are complicated due to the strong interaction between the boundary layer and the reflected shock. These results are independent of the distance from the end wall.

The deceleration of the reflected shock seems to be attributed to the thermal

boundary layer growing on the end wall.[10,11] The shock-heated gas adjacent to the end wall is cooled by a heat transfer to the wall. The gas in the growing thermal boundary layer is relatively dense, and in order to supply the required mass, a displacement velocity toward the wall is induced in the hot gas far away. This flow perturbs the trajectory of the reflected shock wave. Since the shock does not quite stagnate the gas as would happen in an ideal non-heat-conducting case, the velocity jump across the shock is less, so that the shock is weaker. The attenuation of the reflected shock velocity caused by the effect of the thermal boundary layer is 5 % lower than the theoretical value at $M_s=3.45$ and $p_1=0.10$ kPa, and is 3 % at $M_s=2.58$ and $p_1=2.1$ kPa. The effect becomes smaller with a decrease in the Mach number. Hence, it is obvious that the deceleration is caused by not only the thermal layer but also other factor.

The effect of the side-wall boundary layer-reflected shock interaction is not concerned with deceleration, because the results of the shock velocity in air are similar to those in argon, although the behaviour of the reflected shock is different in each case.

On the other hand, it is expected that the shock does not reflect ideally. The velocity ratios of the incident shock to the reflected shock are shown in Figs. 13 and 14. The results agree well with the results obtained by Strehlow and Cohen.[12]

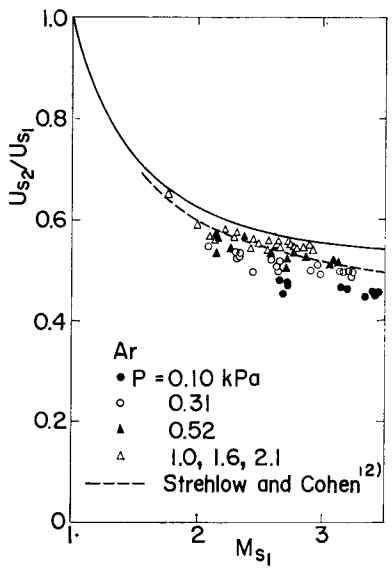

Fig. 13. Velocity Ratio of Incident and Reflected Shocks in Ar.

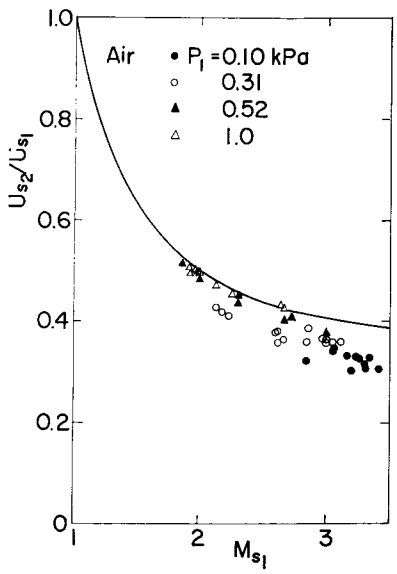

Fig. 14. Velocity Ratio of Incident and Reflected Shocks in Air.

4.2.4. Density Ratio ρ_{52}

The reflected shock density ratio ρ_{21} can be calculated in the same manner as ρ_{21}. The measured values of ρ_{52} are shown in Figs. 15 and 16, where the

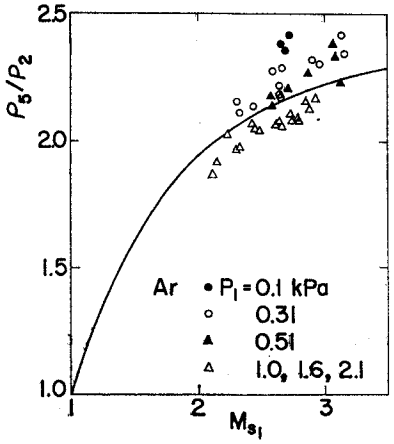

Fig. 15. Reflected Shock Density Ratio ρ_{52} in Ar.

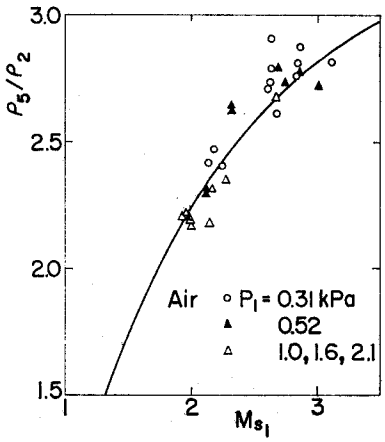

Fig. 16. Reflected Shock Density Ratio ρ_{52} in Air.

solid curves show a theoretical prediction. The values have been taken immediately behind the shock. For $p_1=1.0$ kPa, the measured values are approximately 3.5 % lower than the theoretical values, and they increase with a decrease in the initial pressure. For $p_1=0.10$ kPa, the measured values are 10.5 % above the theoretical curve. These results are contrary to the prediction from the reflected shock velocities shown in Figs. 11 and 13.

For the initial pressure above 1.0 kPa, it is considered that the effect of the boundary layers on the side wall and the end wall are negligible. When the initial pressure is lower, the growth of the boundary layer cannot be neglected, and the temperature T_5 behind the reflected shock is reduced. Consequently, the density ρ_5 behind the reflected shock is elevated. This is the reason why the density behind the reflected shock increases.

The density ρ_5 behind the reflected shock increases gradually. The incident shock is decelerated, and the contact surface is accelerated owing to the side-wall boundary layer. Therefore, the velocity u_2 of the gas behind the incident shock increases with the distance from the shock front, and the gas which is far from the shock is heated by a stronger shock than the observed one. Hence, it is evident that both ρ_2 and ρ_5 increase gradually. The test time i.e. the time difference between the arrival of the shock and that of the contact surface has been measured, and is shown in Fig. 17. The abscisa represents the non-dimensional distance

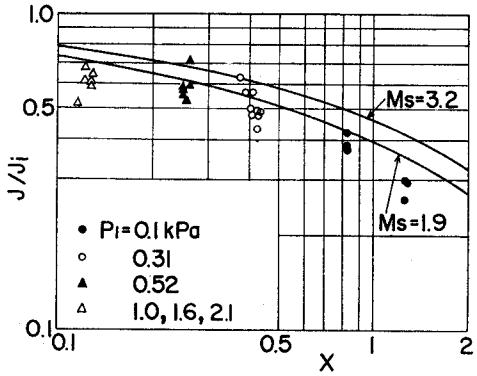

Fig. 17. Measured Test Time.

X from the diaphragm which is non-dimensionalized by $X=x/(l_m\rho_{21})$. Here, l_m is a limiting (maximum) value of the separation distance between the shock and the contact surface, and x is the dimensional distance from the diaphragm. The estimation of l_m was given by Mirels.[13,14] The vertical axis represents the ratio of the test time to the ideal one. The theoretical curves illustrate the estimation by Mirels when the boundary layer is assumed to be laminar. Since the measured values almost agree with the theoretical value, the flow model, where the shock is decelerated and where u_2 is accelerated is reasonable, and therby ρ_2 and ρ_5 are increased.

4.3. Evaluation of the Interferometaer

This interferometer has some advantages and can minimize vibrational sensitivity. The test beam and the reference beam travel through common elements such as common prisms and common lenses. Also, both beams pass through the shock tube so that the vibration is deadened when the diaphragm is broken. The vibration of the floor did not affect the measurements in so far as the sweep time of the oscilloscope is below 100 μs/div.

The spatial resolution depends on the laser beam diameter in a test section. To obtain an optimum spatial resolution, appropriate lenses have to be inserted between the laser and the first Wollaston prism. The minimum confinement of the beam diameter in the test object is given by Eq. (8). PIN-photodiodes have a superior time resolution of nanoseconds.

The differential circuit was adopted as a detector. With this circuit, the laser ripple and beat frequencies can be suppressed to a large extent, so that a high sensitivity is attained. By this interferometer, delicate measurements, i.e. the quantitative determinations of so small an optical path change as 0.2 % of

the beam wave length, are possible.

It is a disadvantage that the signal becomes complicated when the density variation is large. It is to be desired that the main part of the interferometer be set up within a high vacuum vessel, because it is very sensitive to the convection of the surrounding air.

From the facts mentioned above, this interferometer is suitable for quantitative measurements of a very small density change. It is hoped that this interferometer will be a competent means for measuring small density variations, such as the measurement of the density gradient of the flow, the determination of the density profile in a boundary layer etc.

5. Concluding Remarks

The laser differential interferometer using Wollaston prisms was applied to the measurements of the density and the shock velocity in a shock tube.

The physical quantities relating to the incident shock prove to follow the Rankine-Hugoniot relation regardless of the initial pressure. Nevertheless, the reflected shock and the contact surface are influenced by the boundary layer on the side wall behind the incident shock and the thermal boundary layer on the end wall at an initial pressure below 1.0 kPa. The velocity of the reflected shock is decreased and the reflected density ratio ρ_{52} increases. In the case of air, a bifurcation occurs because of the violent interaction between the reflected shock and the boundary layer behind the incident shock. A gradual increase in the density is observed behind the shock.

Through these experiments, a measurement technique by means of this interferometer has been established. The advantages of this interferometer are that the influence of vibration and laser noises is suppressed, that excellent time and spatial resolutions are achieved, that it is suitable for a quantitative determination of very small density variations etc. This is one of the most reliable techniques for gas dynamic investigations.

References

1) G. Smeets, IEEE Transactions on Aerospace and Electronic Systems, Vol. 8, 186 (1972).
2) G. Smeets, *ibid*, Vol. 13, 82 (1977).
3) G. Smeets, Proc. 8th Int. Shock Tube Symp., Chapman and Hall, London, p. 45 (1971).
4) G. Lensch, Doctoral Thesis, Technische Hochschule Aachen (1977).
5) G. Lensch and H. Grönig, Shock Tube and Shock Wave Reserch, University of Washington Press, Seatle, p. 132 (1978).
6) W. Garen and G. Lensch, Shock Tubes and Waves, The Magnes Press, Jerusalem, p. 155 (1980).
7) C. Muckenfuss, Phys. Fluids, Vol. 3, 320 (1960).

8) H.W. Liepmann and R.M. Bowman, Phys. Fluids, Vol. 7, 2013 (1964).
9) H.B. Dyner, Phys. Fluids, Vol. 9, 879 (1966).
10) J.E. Dove and D. McL. Moulton, Proc. Roy. Soc. A 283, 216 (1965).
11) B. Sturtevant and E. Slachmuylders, Phys. Fluids, Vol. 7, 1201 (1964).
12) R.A. Strehlow and A. Cohen, J. Chem. Phys., Vol. 30, 257 (1959).
13) H. Mirels, Phys. Fluids, Vol. 6, 1201 (1963).
14) H. Mirels, AIAA J., Vol. 2, 84 (1964).

Appendix A. Circular Polarization

Consider two harmonious, linearly polarized light waves of the same frequency moving through the same region of space, in the same direction. If they are polarized perpendicularly, the optical disturbances are represented in the form:

$$E_y = A_y \cos(\omega t - kx)\,, \tag{A-1}$$

$$E_z = A_z \cos(\omega t - kx + \phi)\,, \tag{A-2}$$

where ϕ is the relative phase difference between the waves, both of which are traveling in x-direction. From Eqs. (A-1) and (A-2), we have

$$\left(\frac{E_y}{A_y}\right)^2 + \left(\frac{E_z}{A_z}\right)^2 - 2\frac{E_y E_z}{A_y A_z}\cos\phi = \sin^2\phi\,. \tag{A-3}$$

This is the equation of an ellipse. So the end point of the superimposing disturbance traces out an ellipse in a plane perpendicular to the x-axis. If $\phi = (2m+1)\pi/2$ where m is an integer, the principal axes of the ellipse are aligned with the y- and z-axes. Furthermore, if $A_y = A_z$, a circular polarization is realized.

The wave plate is made of birefringent crystal. The axes of the plate are assumed to be aligned with the y- and z-axes, and the refractive indices of the waves oscillating in the x-y plane are n_y, n_z, respectively. The y- and z-components of the incident wave of the linear polarization are represented in the form:

$$E_y = A_y \cos 2\pi\left(\frac{t}{T}\right),$$

$$E_z = A_z \cos 2\pi\left(\frac{t}{T}\right).$$

After traveling through a wave plate with a thickness of d, they are

$$E_y = A_y \cos 2\pi\left(\frac{t}{T} - \frac{n_y d}{\lambda}\right), \tag{A-4}$$

$$E_z = A_z \cos 2\pi\left(\frac{t}{T} - \frac{n_z d}{\lambda}\right). \tag{A-5}$$

The phase difference is then

$$\phi = 2\pi \frac{d}{\lambda}(n_z - n_y) .$$

The thickness of the $\lambda/4$ plate satisfies

$$d(n_z - n_y) = (4m+1)\lambda/4 .$$

If $A_y = A_z = A_0$, Eq. (A-3) reduces to

$$E_y^2 + E_z^2 = A_0^2 .$$

This represents a circular polarization.

Appendix B. Calculation of $p_{\mathrm{bl \cdot stag}}$

In reflected shock coordinates, the side wall moves with the reflected shock velocity U_r, and the temperature of the fluid in the boundary layer is considered to be nearly the same as the wall temperature. Then, as the representative Mach number of the flow in the boundary layer

$$M_{\mathrm{bl}} = \frac{U_r}{a_1} = \frac{2(\gamma-1)M_s^2 + (3-\gamma)}{(\gamma+1)M_s} , \tag{B-1}$$

is reasonable. The stagnation pressure of the flow with the Mach number M_s, and pressure p, is given by

$$p_{\mathrm{stag}}/p = \left(1 + \frac{\gamma-1}{2} M_s^2\right)^{\gamma/(\gamma-1)} . \tag{B-2}$$

The change of the stagnation pressure across the shock is

$$ln \frac{p_{2\cdot\mathrm{stag}}}{p_{\mathrm{bl}\cdot\mathrm{stag}}} = \frac{s_{\mathrm{bl}} - s_2}{R} . \tag{B-3}$$

The change of entropy is given by

$$\frac{s_{\mathrm{bl}} - s_2}{R} = ln \left[1 + \frac{2\gamma}{\gamma+1}(M_{\mathrm{bl}}^2 - 1)\right]^{1/(\gamma+1)} \left[\frac{(\gamma+1)M_{\mathrm{bl}}^2}{(\gamma-1)M_{\mathrm{bl}}^2 + 2}\right]^{\gamma/(\gamma+1)} . \tag{B-4}$$

When $M_{\mathrm{bl}} > 1$, from Eqs. (B-2), (B-3) and (B-4),

$$\frac{p_{\mathrm{bl}\cdot\mathrm{stag}}}{p_2} = \left[1 + \frac{2\gamma}{\gamma+1}(M_{\mathrm{bl}}^2 - 1)\right]^{-1/(\gamma-1)} \left[\frac{\gamma+1}{2} M_{\mathrm{bl}}^2\right]^{\gamma/(\gamma-1)} . \tag{B-5}$$

The relation between M_s and $p_{\mathrm{bl}\cdot\mathrm{stag}}$ is obtained by substituting Eq. (B-1) into Eq. (B-5).